

Chapter 8

Visualization and Segmentation Techniques in 3D Ultrasound Images

Aaron Fenster, Mingyue Ding, Ning Hu, Hanif M. Ladak, Guokuan Li, Neale Cardinal, and Dónal B. Downey

Robarts Research Institute, 100 Perth Drive London, ON,N6A 5K8, Canada,
{afenster,mding,nhu,hladak,mli,cardinal,ddowney}@imaging.robarts.ca

Summary. Although ultrasonography is an important cost-effective imaging modality, technical improvements are needed before its full potential is realized for accurate and quantitative monitoring of disease progression or regression. 2D viewing of 3D anatomy, using conventional ultrasonography limits our ability to quantify and visualize pathology and is partly responsible for the reported variability in diagnosis and monitoring of disease progression. Efforts of investigators have focused on overcoming these deficiencies by developing 3D ultrasound imaging techniques using existing conventional ultrasound systems, reconstructing the information into 3D images, and then allowing interactive viewing of the 3D images on inexpensive desktop computers. In addition, the availability of 3D ultrasound images has allowed the development of automated and semi-automated segmentation techniques to quantify organ and pathology volume for monitoring of disease. In this chapter, we introduce the basic principles of 3D ultrasound imaging as well as its visualization techniques. Then, we describe the use of 3D ultrasound in interventional procedures and discuss applications of 3D segmentation techniques of the prostates, needles, and seeds used in prostate brachytherapy.

8.1 Introduction

Ultrasonography is an inexpensive and safe imaging modality that is widely used for different applications such as material defect detection, and diagnosis and staging of human disease. Conventionally, ultrasound images are two-dimensional (2D) making comprehension of complex three-dimensional (3D) structures and related applications including volume measuring, 3D anatomy display and animation difficult. In order to overcome this problem, 3D ultrasound imaging techniques have been developed in the past decade, which can reconstruct 3D ultrasound images of organs and tissues from acquisition of multiple conventional 2D images.

In Sections 8.2 and 8.3 we address the problems of acquisition and visualization of 3D ultrasound images. In Section 8.4, we introduce the application of 3D US techniques in interventional procedures, such as image-guided surgery

and therapy. Finally, we discuss the use of 3D ultrasound for segmentation techniques used to segment the prostate (Section 8.5), needles (Section 8.6) and brachytherapy seeds (Section 8.7).

8.2 Basic Principles of 3D Ultrasound

Three-dimensional visualization of the interior of the human body has been a goal of diagnostic radiology since the discovery of x-rays. In the 1970s and 1980s, computed tomography (CT), ultrasound (US), positron emission tomography (PET), and Magnetic Resonance Imaging (MRI) have revolutionized diagnostic radiology by providing true 3D information about the interior of the human body. However, 3D visualization techniques were slower to develop, primarily because of the demanding computational requirements for 3D reconstruction and manipulation of the large amount of data in the 3D images. Thus, early systems presented the acquired 3D information as 2D images, requiring the physician to view multiple cross-sections of the anatomy and assemble the 3D information in his or her mind.

Medical ultrasound (US) imaging is a versatile and inexpensive imaging modality available in most hospitals in the world. Current US imaging produces images of high quality, making it an indispensable tool in the management of many diseases, as well as for providing image guidance for interventional procedures. Nevertheless, conventional US imaging still suffers from disadvantages, related to its 2D nature, which 3D imaging attempts to address. Despite decades of exploration, it is only in the past five years that 3D US imaging has advanced sufficiently to move out of the research laboratory and become a commercial product for routine clinical use.

8.2.1 Limitations of 2D US Imaging

The development of 3D US addresses the disadvantages of 2D US imaging that are related to the flexibility and subjectivity of the conventional 2D US exam. Specifically, 3D ultrasound developments address the following limitations:

- Because conventional ultrasound images are 2D, the operators must mentally transform multiple 2D images to develop a 3D impression of the anatomy and pathology during the diagnostic examination or during an image-guided interventional procedure. This imaging approach is time-consuming, inefficient, requiring an experienced operator, and can potentially lead to incorrect diagnostic or therapeutic decisions.
- Staging and planning of interventional procedures often requires accurate estimation of organ or tumor volumes. Current 2D US volume measurement techniques assume an idealized shape, and use only simple measures of the width and length in a few views. This practice leads to inaccuracy and operator variability in volume estimation.

- During interventional procedures and in monitoring the results of therapy, it is important to obtain the same views repeatedly. However, it is difficult to localize the thin 2D US image plane to a particular feature in the organ, and more difficult to reproduce the same image location and orientation later, making conventional 2D US imaging nonoptimal for the quantitative monitoring of interventional techniques or for follow-up studies for monitoring the effects of therapy.
- The patient's anatomy or position sometimes restricts the image angle attainable with the US transducer, resulting in inaccessibility of the optimal image plane necessary for diagnosis or image-guided therapy.

8.2.2 Requirements for 3D US Imaging

The most common 3D US approach makes use of conventional ultrasound machines and transducers with 1D arrays. These transducers are manipulated in various ways to produce multiple 2D images, which are then reconstructed into 3D images. Because the 3D images are produced from a series of 2D images, their relative positions and orientations must be accurately known, so that the reconstructed 3D image is not distorted.

Three approaches have been used to produce 3D US images with conventional 2D US systems: tracked freehand, untracked freehand, and mechanical assemblies. A fourth approach has been developed in which 2D arrays are used to produce 3D US images directly. In the following sections, we briefly describe these approaches and describe segmentation techniques for 3D US based planning and guidance of interventional procedures. For detailed descriptions of 3D ultrasound imaging approaches, the reader can refer to recent review articles and a book [1, 2, 3].

8.2.3 3D US Scanning Mechanisms

2D Arrays

To produce 3D images in real time, systems using 2D arrays keep the transducer stationary, and use electronic scanning to sweep the US beam over the anatomy. The system developed at Duke University for real-time 3D echo cardiography has shown the most promise, and has been used for clinical imaging [4, 5]. The transducer is composed of a 2D array of elements, which are used to transmit a broad beam of ultrasound diverging away from the array and sweeping out a pyramidal volume. The returned echoes are then detected by the 2D array and processed to display multiple planes from the volume in real time. These planes can then be interactively manipulated to allow the user to view the desired image region.

Mechanical Assemblies

Instead of using 2D arrays to produce 3D images, conventional transducers with 1D arrays can be used to scan the desired anatomical volume. As the transducer is swept across the volume, the series of 2D images produced by the conventional US system is recorded rapidly. If mechanical assemblies are used to move the transducer in a precisely predefined manner, the relative position and orientation of each 2D image can be accurately known, and the acquired series of 2D images can therefore be reconstructed into a 3D image.

Numerous mechanical scanning assemblies have been developed, in which the transducer is made to rotate or translate by a motor. The mechanical assemblies vary in size from small, integrated probes that house the mechanical mechanism, to larger external mounting mechanical assemblies.

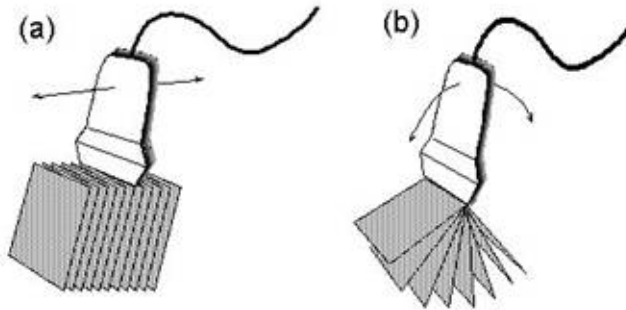


Figure 8.1. Diagram showing two 3D US mechanical scanning approaches: (a) linear motion, and (b) tilt motion. In both cases, the 2D images are acquired with constant spatial or angular spacing.

The integrated mechanical 3D scanning systems are easy for the operator to use, but are larger and heavier than conventional transducers. In addition, they require a special ultrasound machine, and cannot be used with any other conventional ultrasound systems. The external mounting assemblies are generally bulkier, but can be adapted to any conventional US machine. Different types of mechanical assemblies have been used to produce 3D images, as shown schematically in Figure 8.1.

Linear Motion: The transducer is mounted in a mechanical assembly which is translated linearly over the patient's skin, as shown in Figure 8.1(a),

so that the set of 2D images acquired parallel to one another at a known spatial interval. Because the scanning geometry is known, the 3D reconstruction parameters can be precomputed, resulting in the 3D image being available for viewing immediately after the scan is performed [6].

Because the resolution in the acquired 2D images is nonisotropic, the resolution in the reconstructed 3D image produced by linear scanning will also be nonisotropic. Because conventional transducers have poor elevational resolution, the resolution in the scanning direction will be the worst. However, the resolution will be unchanged in the planes corresponding to the original 2D images.

This approach has been used successfully in many vascular applications, including B-mode [6, 7, 8], color Doppler imaging of the carotid arteries [7, 9, 10, 11, 12], tumor vascularity [13, 6], test phantoms [9, 14], and power Doppler imaging [6, 7, 9].

To avoid distortions in the reconstructed 3D images, Cardinal et al. [15] have shown that the distance between the acquired 2D images, and the tilt angle of the 2D image planes with respect to the scanning direction must be known accurately. To ensure that the error in volume measurements is less than 5%, the distance between acquired images must be less than 0.05 mm for a spacing of 1 mm.

Tilt Motion: The transducer is mounted in a mechanical assembly and tilted about an axis parallel to the face of the transducer, as shown in Figure 8.1(b). The tilting axis can be either at the face of the transducer, producing a set of 2D images that intersect at the face, or above it, causing the set of 2D planes to intersect above the skin. This approach allows the transducer face or the 3D probe housing to be placed at a single location on the patient's skin, making it useful for a wide range of abdominal ultrasound imaging applications [16, 7, 17].

This scanning approach has also been used successfully with endocavity transducers, such as transesophageal (TE) and transrectal (TRUS) transducers. In these applications, a side-firing linear array is used with either an external fixture or an integrated 3D transducer. The transducer is rotated about its long axis while 2D images are acquired. After a rotation of about 100, the acquired 2D images are arranged in fanlike geometry similar to that shown in Figure 8.1(b). This approach has been used successfully to image the prostate for diagnostic applications (Figure 8.2) [6, 7, 18, 19], and for 3D US-guided cryosurgery and brachytherapy [20, 6]. The main advantage of the tilt scanning approach is that the 3D scanning mechanism can be made compact to allow easy hand-held manipulation. In addition, using a suitable choice of scanning angle and angular interval, the scanning time can be short. Because the set of planes is acquired with a predefined angular interval, geometric 3D reconstruction parameters can be precalculated, allowing immediate viewing of the 3D image.

Because the acquired 2D images are arranged in a fanlike geometry, the distance between the planes will increase with distance from the trans-

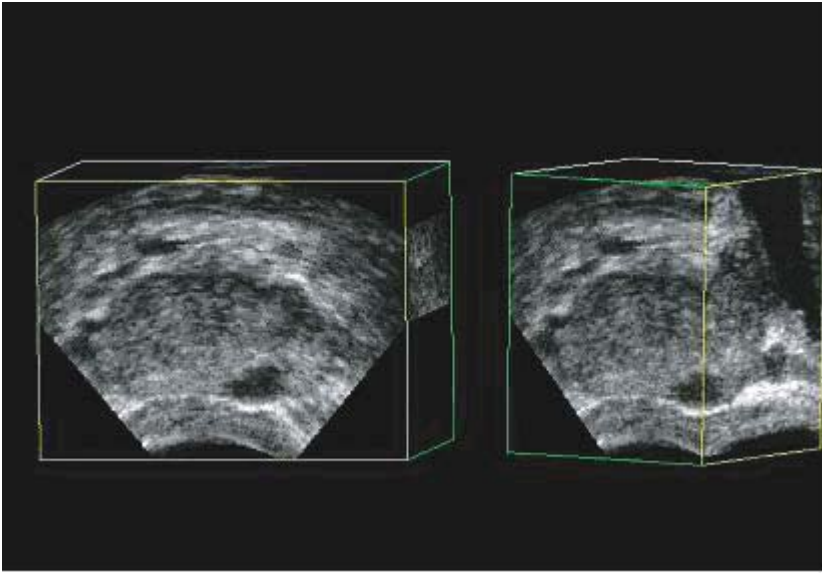


Figure 8.2. Two multiplanar rendering views of a 3D US image of a prostate with a carcinoma obtained with a mechanical tilt scanning approach.

ducer (rotation axis). However, the change with distance in the sampling interval can be approximately matched to the change with distance of the elevational resolution, thereby minimizing the effect of spatial sampling degradation. In combination, these two effects make the resolution worst in the scan (tilt) direction, and degrade with distance from the transducer. Tong et al. [21] have reported on an analysis of the linear, area, and volume measurement errors for the mechanical tilting transducer approach. They showed that if the location of the axis of rotation is known exactly, then the percentage error in volume will equal the percentage error in the rotation angle. To ensure a volume error of less than 5% for a typical scanning angle of 100, the total accumulated error in the scan angle must be less than 5. Thus, for a scan containing 100 2D images, the systematic error in the angular interval between images must be less than 0.05.

Tracked Free-Hand Scanning

Although mechanical scanning approaches result in geometrically accurate 3D images, the mechanical assemblies are generally bulky and at times inconvenient to use. To overcome this problem, free-hand scanning approaches have been developed that allow the user to manipulate the transducer freely by hand without significant constraints. While the anatomy is being scanned, the positions and orientations of the acquired 2D images are tracked and recorded, so that the 3D image can be reconstructed. Because the scanning geometry is

not predefined, the operator must ensure that the set of acquired 2D images has no significant gaps. Several free-hand scanning approaches have been developed, which use four basic position-sensing techniques: acoustic tracking, articulated arms, magnetic field tracking, and image-based information.

Acoustic Tracking: In this approach, sound-emitting devices (spark gaps) were mounted on the transducer, and an array of fixed microphones was mounted above the patient. As the operator moved the transducer over the patient's skin in the usual manner, the 2D ultrasound images were continuously acquired, and the acoustic pulses from the sound emitters were continuously recorded by the microphones. Using the speed of sound in air and the time-of-flight of the acoustic pulses from the emitters to the microphones, the positions and orientations of the acquired 2D images were then determined [22, 23].

Articulated Arms: A partially constrained free-hand scanning approach was achieved by scanning the patient with the transducer mounted on a multi-jointed mechanical arm system. The relative rotation of the arms was measured with potentiometers located at each joint, and the relative positions and orientations of the acquired 2D images were calculated. While the transducer was manipulated over the patient's anatomy, a computer recorded the acquired 2D images and the relative orientation of all the arms, which were then used to reconstruct the 3D image.

Magnetic Field Tracking: The most successful free-hand scanning approach makes use of a six degree-of-freedom magnetic field sensor to track the ultrasound transducer. In this approach, a transmitter is used to produce a spatially varying magnetic field, and a small receiver containing three orthogonal coils mounted on the transducer is used to sense the magnetic field strength. By measuring the strength of three components of the local magnetic field, the US transducer's position and orientation can be continuously monitored.

Although magnetic field sensors are small and unobtrusive, their accuracy can be compromised by electromagnetic interference from sources such as CRT monitors, AC power cabling, and some electrical signals from ultrasound transducers. Also, ferrous and highly conductive metals can distort the magnetic field, causing geometric errors in the tracking information. However, by ensuring that the immediate scanning environment is free of electrical interference and metals, high quality 3D images can be obtained [24, 25, 26, 27, 28, 29, 30].

Speckle Decorrelation: Free-hand scanning techniques described above require an external sensor to measure the relative positions and orientations of the acquired 2D images. However, the relative positions of adjacent 2D images can also be measured using the well-known phenomenon of speckle decorrelation. When a source of coherent energy interacts with scatterers, the reflected spatial energy pattern will appear as a speckle pattern. This speckle is characteristic of US images and can be used in 3D US imaging.

If two 2D US images are acquired from the same location and orientation, then their speckle patterns will be the same. However, if one image is acquired a short distance away from the other, then the degree of decorrelation in the speckle will be proportional to the distance between the two images [31]. Since the relationship between the degree of decorrelation and distance will depend on several transducer parameters, accurate determination of the separation of the images requires calibration of the relationship between distance and various transducer parameters.

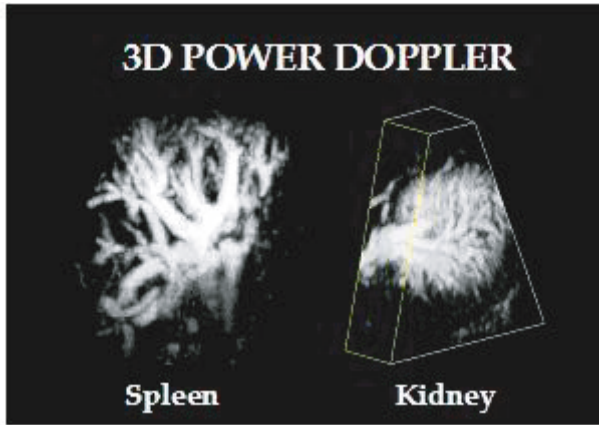


Figure 8.3. Two 3D power Doppler images obtained with free-hand scanning without position sensing and displayed using volume rendering. On the left is a spleen and on the right, a kidney.

Untracked Free-Hand Scanning

In this approach, the operator moves the transducer in a steady motion, while a series of 2D images are acquired. Because the position and orientation of the transducer are not recorded, the linear or angular spacing between the acquired images is assumed in the reconstructing 3D image. Thus, geometric measurements such as distance or volume may still be inaccurate. If the transducer's motion is uniform and steady, then very good 3D images may be reconstructed, as illustrated by Figure 8.3 [7].

8.3 3D US Image Reconstruction

Reconstruction of 3D US images refers to the process of placing the acquired 2D images into the 3D image in their correct relative positions. Two methods have been used: feature-based and voxel-based reconstruction.

8.3.1 Reconstruction of Features

In this approach, each acquired 2D image is segmented and classified into the desired features that are to be reconstructed. Typical examples have been implemented by manually or automatically outlining of the boundaries of the ventricles in echocardiographic images or of the fetus in obstetrical images. The boundary of each structure is then represented by a mesh and displayed.

The advantage of this reconstruction approach is that the 3D image is reduced to a description of surfaces in the form of a mesh, enabling the use of common hardware and software tools to manipulate and display these surfaces in real time. The main disadvantage of this approach relates to the segmentation and classification process, which identifies and stores information only about the anatomical boundaries. Thus, important anatomical information is lost, such as subtle pathological features related to tissue image texture.

8.3.2 Reconstruction of a Cartesian Volume

The most common 3D US reconstruction approach uses the set of acquired 2D images to build a 3D grid of voxels. This is accomplished by placing the pixels in the acquired 2D images into their correct locations within the 3D image. The values (color or grayscale) of the voxels not sampled are calculated by interpolation from their nearest neighbors. In this approach, all the original information is preserved in the 3D image, and the original 2D images can be recovered. However, if the angular or spatial spacing between the acquired 2D images is not chosen properly, the scanning process will not sample the volume adequately, resulting in degradation of resolution in the reconstructed 3D image. Sampling the volume properly and avoiding gaps results in large image files that can range from 16 MB to 96 MB [32, 6].

8.3.3 Viewing 3D US Images

Multiplanar Reformatting: Cube View

The most common approach for viewing 3D US images is based on multiplanar reformatting (MPR) of the 3D image. In the cube view approach, the 3D image is presented as a polyhedron, and the appropriate 2D US images are “painted” on each face by texture mapping (Figures 8.2 and 8.4). The polyhedron can be rotated and any face may be moved, either parallel or obliquely to its original location, while the appropriate US data is continuously texture-mapped in real time onto the new face. Thus, the operator always has 3D image-based cues relating the plane being examined to the rest of the anatomy [11, 19, 2].

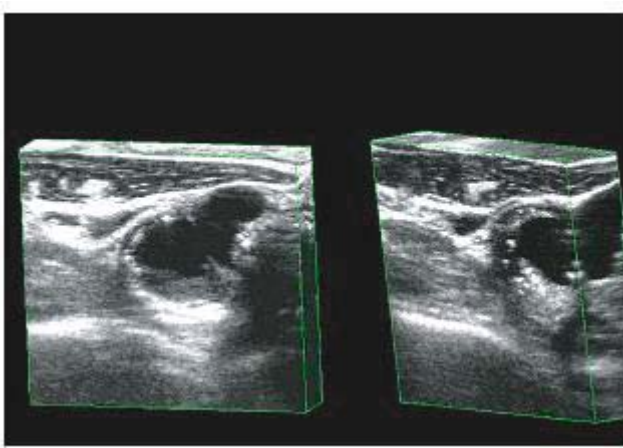


Figure 8.4. Two multi-planar rendered views of a 3D US image of the carotid arteries with a plaque at the entrance to the internal carotid artery.

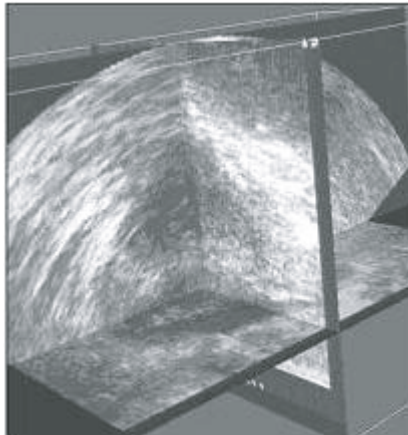


Figure 8.5. A 3D US image of a prostate displayed using the MPR technique as intersecting orthogonal planes.

MPR: Orthogonal Planes

In this MPR approach, three perpendicular planes are displayed simultaneously, with graphical cues indicating their relative orientations (Figure 8.5). For easier appreciation, these planes are typically made perpendicular to each other. User interface tools are provided to allow the operator to select any plane, and move it parallel or obliquely to the original, to provide the desired view of the anatomy [33, 34, 2].

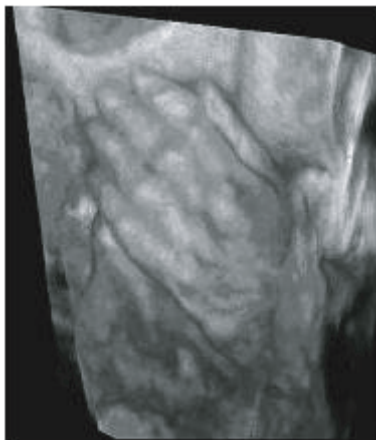


Figure 8.6. 3D US image displayed using the VR technique showing a fetal hand.

Volume Rendering (VR)

The volume rendering technique presents a display of the entire 3D image after projection onto a 2D plane. Image projection is typically accomplished via ray-casting techniques [35]. Although many VR algorithms have been developed, 3D US imaging currently makes use of primarily two approaches: maximum (minimum) intensity projection, and translucency rendering. This approach has been primarily used to display fetal (Figure 8.6) and vascular anatomy (Figure 8.3)[7].

8.4 3D US-Guided Prostate Brachytherapy

Prostate cancer is the most commonly diagnosed malignancy in men over 50, and was found at autopsy in 30% of men at age 50, 40% at age 60, and almost 90% at age 90 [36]. However, when it is correctly diagnosed at an early stage, prostate cancer is curable, and even at later stages, surgical treatment can still be effective.

One of the most promising options for treatment of early prostate cancer is prostate brachytherapy, which is used to implant 80–100 radioactive seeds (e.g., ^{125}I or ^{103}Pd) in or near the prostate and avoid radiation-sensitive normal-tissue structures [37]. Because the radiation dose produced by each seed falls off rapidly with distance, the correct positioning of the seeds is crucial to the success of the procedure. For each patient, an implantation dose preplan is generated based on a CT or 3D US image of the prostate. During a later outpatient procedure, the patient is positioned in approximately the same position as for the preimplantation image, and brachytherapy seeds are

then implanted in the prescribed positions using a needle. Real-time transrectal US (TRUS) is used to ensure accurate placement of the seeds.

Because of possible changes in prostate size and shape between the preimplantation and implantation procedures, as well as possible changes in the patient position between the preimplantation and implantation images, errors in seed placement can occur. Performing preimplant dose planning and seed implantation during the same session could avoid these problems. This could be done by using a 3D US imaging system with rapid scanning and immediate viewing of the 3D prostate anatomy. In addition, this system could be used to provide improved image guidance during the procedure. Thus, an efficient brachytherapy procedure could be achieved by integrating 3D US imaging with the accurately determined positions of the prostate, needles and seeds.

In the following discussion, we review prostate, needle, and seed segmentation techniques developed by the investigators and present the most novel technique in details.

8.5 Prostate Segmentation in 3D US Images

In prostate brachytherapy, assigning the appropriate therapy dose requires accurate knowledge of the prostate shape and its volume. Traditionally, this is done via manual planimetry, which not only is time-consuming and tedious to perform, but also highly operator dependent, causing variability in the results. In order to determine the shape of the prostate and measure its volume more accurately and consistently, an automated or semi-automated technique is required.

8.5.1 Previous Work

Most currently available prostate segmentation algorithms focus on segmentation of 2D US images. [38] proposed the Laplacian-of-Gaussian edge operator followed by an edge-selection algorithm, which requires the user to select several initial points to form a closed curve. Their method correctly identified most of the boundary in a 2D US prostate image. This technique was extended using four texture energy measures associated with each pixel in the image [39]. An automated clustering procedure was used to label each pixel in the image with the label of its most probable class. Although good results were reported for 2D US prostate images, the algorithm was computationally intensive, requiring about 16 minutes to segment the prostate boundary in 2D with a 90-MHz SUN SPARCstation.

Aarink et al. [40, 41, 42, 43] published a series of papers on prostate segmentation. First, they used cross-sections of the prostate obtained with a well-defined distance. In each image, the contour of the prostate was determined using edge detection techniques. After locating the prostate, the area

of the prostate was calculated for each image and the volume of the prostate was determined by multiplying the summation of these areas by the distance between the cross-sections. In 1994, they proposed a practical clinical method to determine the 2D prostate contour, which comprised three steps: edge detection, edge enhancement and selection, and edge linking by interpolation. Although they reported good segmentation results in 1996, their method could not ensure robust and accurate segmentation due to the speckled noise and image shadows.

In 1997, Liu et al. [44] presented an algorithm based on their radial bas-relief (RBR) edge detector. First the RBR detector highlighted the edges in the image, and then binary processing and area labeling were used to segment the boundary. Their results showed that RBR performed well with a good-quality image, and marginally for poor-quality images. The RBR approach was able to extract a skeletonized image from an US image automatically. However, many spurious branches were created introducing ambiguity in defining the actual prostate boundary. In 1998, Kwok et al. (1998) [45] extended the RBR technique by fitting a Fourier boundary representation to the detected edges, resulting in a smooth boundary, but this technique required careful tuning of algorithm parameters.

Pathak et al. [46, 47, 48] also developed an edge guidance delineation method for deformable contour fitting in a 2D ultrasound image and statistically demonstrated a reduction in the variability in prostate segmentation.

In 1999, Knoll et al. [49] proposed a technique for elastic deformation of closed planar curves restricted to particular object shapes using localized multiscale contour parameterization based on the wavelet transform. The algorithm extracted only important edges at multiple resolutions and ignored other information caused by noise or insignificant structures. This step was followed by a template-matching procedure to obtain an initial guess of the contour. This wavelet-based method constrained the shape of the contour to predefined models during deformation. They reported that this method provided a stable and accurate fully automatic segmentation of 2D objects in ultrasound and CT images.

In 2001, Garfinkel et al. [50] used a deformable model to segment the prostate from 3D US images. Their approach required the user to initialize the model by outlining the prostate in 40–70% of the 2D slices of each prostate, using six to eight vertices for each 2D contour, and then an initial 3D surface was generated. The running time of the algorithm was about 30 sec on a SUN Ultra 20. They compared algorithm and manual segmentation results by computing the ratio of the common pixels that were marked as prostate by both methods. The results showed an accuracy of nearly 89% and a three- to six-fold reduction in time compared to a totally manual outlining. No editing of the boundary was possible to improve the results.

Although a variety of segmentation methods have been proposed, none segments the prostate in the 3D US image directly and allows editing of the results. Without the use of a complete 3D prostate image, prostate shape in-

formation is not used efficiently, leading to an inaccurate and time-consuming segmentation. To overcome this shortcoming, an alternative direct 3D segmentation method is more promising.

In this section, we describe a semi-automatic 3D prostate segmentation approach, which uses an ellipsoid 3D mesh model of the prostate to initialize the procedure, and used the discrete dynamic contour (DDC) approach to refine the contour in 3D. Experiments demonstrated that the average difference between our algorithm and manually segmented 3D prostate boundaries varied from 0.08 mm to 0.5 mm while, the volume difference varied from 6% to 10%. The computational time for the whole 3D prostate is about 60 sec on a Pentium III 400-MHz PC computer.

8.5.2 3D Prostate Segmentation Based on the Deformable Ellipsoid Model

The deformable model, also called the snake or active contour, was first proposed by Kass *et al.* in 1987 [51, 52], and has become a widely used technique in medical image analysis [53, 54, 55, 56, 57, 58, 59, 60].

Miller *et al.* [61] extended this technique and developed a geometrically deformable model, which was further extended by Lobregt and Viergever to the discrete dynamic contour [62]. They used force analysis at contour vertices to replace the energy minimization of the whole contour so that a boundary was found by driving an initial contour to the true object boundary. Because the internal and external forces are evaluated only at the vertices, instead of the trajectory of the connected edge segments, the DDC method is much faster than the traditional deformable model approach.

In our previous paper [63], we reported on the development of an algorithm to fit the prostate boundary in a 2D image using the DDC with model-based initialization. A cubic interpolation function was used to estimate the initial 2D contour from four user-selected points, which was then deformed automatically to fit the prostate boundary. However, diagnosis and therapy planning of prostate cancer typically require the prostate volume and its 3D shape. Constructing a 3D prostate boundary from a sequence of 2D contours can be time-consuming or subject to errors.

Based on the 3D triangle mesh deformable model [64], we developed a deformable ellipsoid model for 3D prostate segmentation. It comprises three steps: (1) 3D mesh initialization of the prostate using an ellipsoid model; (2) automatic deformation to refine the prostate boundary; and (3) interactive editing of the deformed mesh, after which step 2 is repeated.

Initialization

In order to initialize the prostate mesh, the user manually selects six control points (x_n, y_n, z_n) , $n = 1, 2, \dots, 6$, on the “extremities” of the prostate in the 3D US image. Typically, the user selects an approximate central transverse

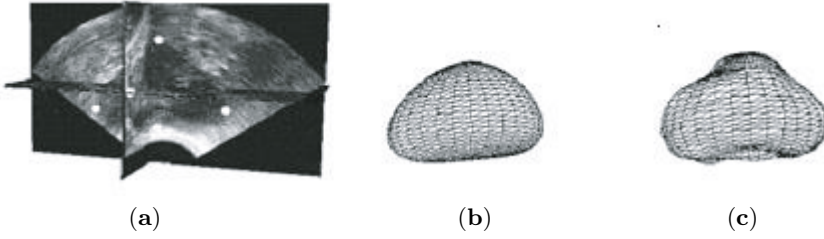


Figure 8.7. 3D prostate segmentation using the deformable ellipsoid model: (a) 3D US image with five of the six user-selected control points shown in white, (b) initial mesh, (c) final deformed mesh.

prostate cross-section and then places two points near the prostate's lateral extremes and two near its top and bottom on the central axis. The last two points are placed near the prostate's apex and base. A 3D US prostate image with five of the six initialization points is shown in Figure 8.7(a). These control points are used to estimate an initialization ellipsoid, which is parameterized as follows [65]:

$$\mathbf{r}(\eta, \omega) = \begin{bmatrix} x \\ y \\ z \end{bmatrix} = \begin{bmatrix} x_0 + a \cos(\eta) \cos(\omega) \\ y_0 + b \cos(\eta) \sin(\omega) \\ z_0 + c \sin(\eta) \end{bmatrix}, \quad -\frac{\pi}{2} \leq \eta \leq \frac{\pi}{2}, -\pi \leq \omega \leq \pi, \quad (8.1)$$

where (x_0, y_0, z_0) is the center of the ellipsoid and a, b , and c are the lengths of the semi-major axes in the x , y , and z directions, respectively. The length, width, and height of the prostate are assumed to be approximately oriented along the x -, y -, and z -axes of the 3D US image, as shown in Figure 8.7(a). First, from the pair of control points with extreme x values, we estimate x_0 as half the sum the x coordinates and a as half the absolute difference. Similarly, we estimate y_0 and b from the pair with extreme y values, and z_0 and c from the pair with extreme z values. The vector $\mathbf{r}(\eta, \omega)$ then describes the surface coordinates of the ellipsoid as a function of the azimuthal angle ω and elevational angle η , defined in the usual manner with respect to the x -axis and the x - y plane. Thus, by stepping the angles ω and η through an appropriate grid of angular values, a set of regularly spaced points is obtained on the surface of the ellipsoid. The ellipsoid's surface is then represented by a mesh of triangles connecting these points [66].

Usually, the ellipsoid generated as described above does not pass through the six control points, nor does it fit the prostate boundary very well. To obtain a better fit, the ellipsoid is warped using the thin-plate spline transformation [67]. Using this transformation, the six ends of the ellipsoid's major axes are mapped onto the corresponding control points. The resulting mesh, as shown in Figure 8.7(b), then becomes the initial mesh for the deformation step.

Contour Deformation

The process for finding the 3D prostate boundary is almost identical to the 2D segmentation technique described by [63], but extended to 3D by calculating the internal force \mathbf{f}_i^{int} acting on each vertex i from Equation (8.2)

$$\mathbf{f}_i^{int} = \left(\left(\frac{1}{6} \sum_j \hat{e}_{ij} \right) \cdot \hat{\mathbf{r}}_j \right) \cdot \hat{\mathbf{r}}_i \quad (8.2)$$

$$e_{ij} = p_i - p_j \quad (8.3)$$

where e_{ij} is the edge vector pointing towards vertex i from one of its six neighboring vertices j , and $\hat{\mathbf{r}}$ denotes the unit radial vector at vertex i . These equations are iterated until either all the vertices have reached equilibrium, or the number of iterations has reached a preset limit. In our experiment, we found that sufficient accuracy was generally achieved within 40 iterations (see Figure 8.7(c)).

Contour Editing

The initialization procedure may place some mesh vertices far from the actual prostate boundary. The deformation process may not drive these vertices towards the actual boundary because the image force exerts a strong effect only near the edge of the prostate, where the image intensity changes rapidly. In these cases, the user can edit the mesh by dragging a vertex to its desired location. To avoid rapid transition in the boundary, adjoining vertices within a user-defined radius are also automatically deformed using the thin plate spline transformation. After editing, the automatic deformation process resumes, with the iteration count reset to zero.

8.6 Needle Segmentation in 3D US Images

8.6.1 Introduction

As discussed in Section 8.4, brachytherapy radioactive seeds are delivered by an implantation needle as it is withdrawn. Although the needle insertion can be guided with a real-time 2D US imaging system, it is our experience from prostate cryosurgery [20] that the 3D trajectory of the needle cannot be fully ascertained, because lateral deflection is poorly detected. However, in order to use 3D US guidance to overcome this problem, it is necessary to be able to segment the needle in the 3D US image, in near real time. This task is made difficult by artifacts in the US image caused by speckle, shadowing, refraction, and reverberation, and by the low contrast of the needle when it is not parallel to the US transducer. Because of these difficulties, traditional local operators

such as edge detectors are inadequate for finding the needle boundary. The challenge is to find a needle segmentation approach that is insensitive to these image artifacts, yet is fast, accurate, and robust.

In this section, we describe just such an approach, which also requires minimal manual initialization. This approach is motivated by four observations: (1) the needle image lies along a straight line; (2) the needle is more conspicuous in a projection image than in the original 3D US image; (3) after segmenting the needle in a 2D projection image, we know that the needle lies in the plane defined by two vectors: the projection direction and the needle direction in the projection image; (4) therefore, if we use two orthogonal projections, we know that the needle must lie along the intersection of the two corresponding planes.

Our approach is composed of four steps: (1) volume cropping, using a priori information to restrict the volume of interest; (2) volume rendering, to form the 2D projection images; (3) 2D needle segmentation, in a projection image; and, (4) 3D needle segmentation, or calculation of the 3D needle endpoint coordinates.

Experiments with US images of both agar and turkey breast test phantom (see Figure 8.8) demonstrated that our 3D needle segmentation method could be performed in near real time (about 10 frames-per-second with a 500 MHz personal computer equipped with a commercial volume-rendering card to calculate the 2D projection images). The root-mean-square accuracy in determining needle lengths and endpoint positions was better than 0.8 mm, and about 0.5 mm on average, for needle insertion lengths ranging from 4.0 mm to 36.7 mm.

8.6.2 Volume cropping

The 3D US image is usually large with displays complex echogenicity (see Figures 8.8 and 8.9 (a)). These attributes result in increased computational time required to perform the image segmentation. In addition, they also increase the likelihood that some background structures have a similar range of voxel intensities as the needle voxels, increasing the difficulty of segmenting the needle. Even in a 2D projection (volume-rendered) image, in which a background structure overlaps that of the needle, automatic segmentation of the needle is much more difficult. However, if background structures are well separated from the needle in the 3D US image, volume cropping can effectively alleviate this problem. Furthermore, cropping will also reduce the size of the volume to be rendered, significantly reducing computation time.

Based on a priori information about the needle location and orientation, volume cropping restricts the volume of interest to the 3D region that must contain the needle. This information is composed of the approximate insertion point, insertion distance, insertion direction, and their uncertainties. This information can be made available when the needle is inserted manually or by a motorized device under computer control, or whenever it is localized using

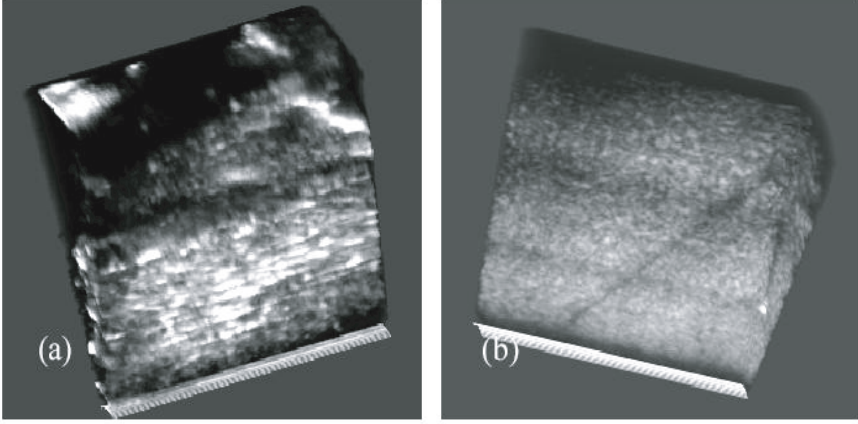


Figure 8.8. Views of 3D US images of the two types of phantoms used to experimentally evaluate our automatic needle segmentation algorithm. The 3D images are displayed using the multi-planar technique: (a) agar, (b) turkey breast.

an acoustic, articulated arm, electromagnetic, or optical tracking device [36]. Our approach proceeds as follows.

Let $\mathbf{L}'_1 = (x'_1, y'_1, z'_1)$ and $\mathbf{L}'_2 = (x'_2, y'_2, z'_2)$ be the 3D image coordinates of the needle's insertion point and end point, respectively, and let $\mathbf{L}'_0 = |\mathbf{L}'_2 - \mathbf{L}'_1|$ be its inserted length. Then the 3D needle vector from insertion point to tip can be written as $\mathbf{L}'_0 = \mathbf{L}'_2 - \mathbf{L}'_1 = L'_0 \mathbf{P}'$, where the unit vector \mathbf{P}' is the needle direction. We then assume that the uncertainty in the needle insertion point can be estimated and that $x'_1 = x_1 \pm \Delta x$, $y'_1 = y_1 \pm \Delta y$, $z'_1 = z_1 \pm \Delta z$, $L'_0 \leq L_0$, and that the angle between \mathbf{P}' and a given approximate needle direction $\mathbf{P} = (a, b, c)$ is at most $\phi < \pi/2$. Then every needle voxel (x, y, z) must lie within the cropped volume defined by the 3D range:

$$[x_{\min}, x_{\max}] \times [y_{\min}, y_{\max}] \times [z_{\min}, z_{\max}] \quad (8.4)$$

where

$$x_{\min} = \min(x_1 - \Delta x, x_1 - \Delta x + (a - 2 \sin(\phi/2)) \cdot L_0), \quad (8.5)$$

$$x_{\max} = \max(x_1 + \Delta x, x_1 + \Delta x + (a + 2 \sin(\phi/2)) \cdot L_0), \quad (8.6)$$

$$y_{\min} = \min(y_1 - \Delta y, y_1 - \Delta y + (b - 2 \sin(\phi/2)) \cdot L_0), \quad (8.7)$$

$$y_{\max} = \max(y_1 + \Delta y, y_1 + \Delta y + (b + 2 \sin(\phi/2)) \cdot L_0), \quad (8.8)$$

$$z_{\min} = \min(z_1 - \Delta z, z_1 - \Delta z + (c - 2 \sin(\phi/2)) \cdot L_0), \quad (8.9)$$

$$z_{\max} = \max(z_1 + \Delta z, z_1 + \Delta z + (c + 2 \sin(\phi/2)) \cdot L_0). \quad (8.10)$$

An example of volume cropping is given in Figure 8.9(b).

8.6.3 Volume rendering

Volume rendering is used extensively in exploring 3D images. In this process, projection images are generated by casting parallel (or divergent) rays through a 3D image volume, where they accumulate both luminance $c(I)$ and opacity $\lambda(I) \leq 1$ as a function of the local voxel intensity I [68]. The grayscale intensity of the projected 2D image plane is then the final accumulated luminance C after the ray has passed through the volume. In general, the projected 2D image of the needle will have the greatest contrast when both of the functions $c(I)$ and $\lambda(I)$, called the transfer functions, match the distribution of I in the needle voxels. Using phantom test objects, we found that this distribution could be accurately modelled as a Gaussian distribution with mean \bar{I} and standard deviation σ_I , where the parameters \bar{I} and σ_I depend on the image appearance of the object. In our experiments, we defined the transfer functions as

$$C(I) = \lambda(I) = \exp\left(-\frac{1}{2}\left(\frac{I - \bar{I}}{\sigma_I}\right)^2\right). \quad (8.11)$$

Using these Gaussian transfer functions, the 2D projection image is then specified by the projection direction, which in our case is always perpendicular to the a priori approximate needle direction \mathbf{P} .

8.6.4 2D Needle Segmentation

In the 2D projection image, we initially search for objects (connected groups of pixels) with pixel intensities exceeding a fixed threshold of 25 (on an 8-bit scale of 0 to 255). This threshold was chosen experimentally to include virtually all needle pixels, while excluding most non-needle pixels. Because of the volume cropping operation, we may safely assume that the object with the largest extent in the \mathbf{P} direction is the needle. (We note that, because the projection direction is always chosen perpendicular to \mathbf{P} , the vector \mathbf{P} always lies in the projected image plane.) Then, using a flood-fill algorithm, the pixels in this object are assigned a value of 1, while all other pixels are assigned a value of 0, resulting in a binary 2D projection image of the needle as shown in Figure 8.9(d).

We assume that the projection image has 2D Cartesian coordinates (u, v) , chosen so that $\hat{u} = \mathbf{P}$. Then, the projected needle image lies within an angle $\phi < \pi/2$ of the u -axis, so we can perform a least-squares fit of the binary projected needle image, to find the estimated projected needle vector \mathbf{L} . With knowledge of the needle direction, we determine its endpoints (u_1, v_1) and (u_2, v_2) , with $u_1 < u_2$, so that (u_1, v_1) corresponds the needle's insertion point and (u_2, v_2) corresponds to its end point.

8.6.5 3D Needle Segmentation

Given the a priori approximate needle direction \mathbf{P} , we define two other unit vectors \mathbf{Q} and \mathbf{R} such that $\{\mathbf{P}, \mathbf{Q}, \mathbf{R}\}$ are mutually orthogonal, and form the

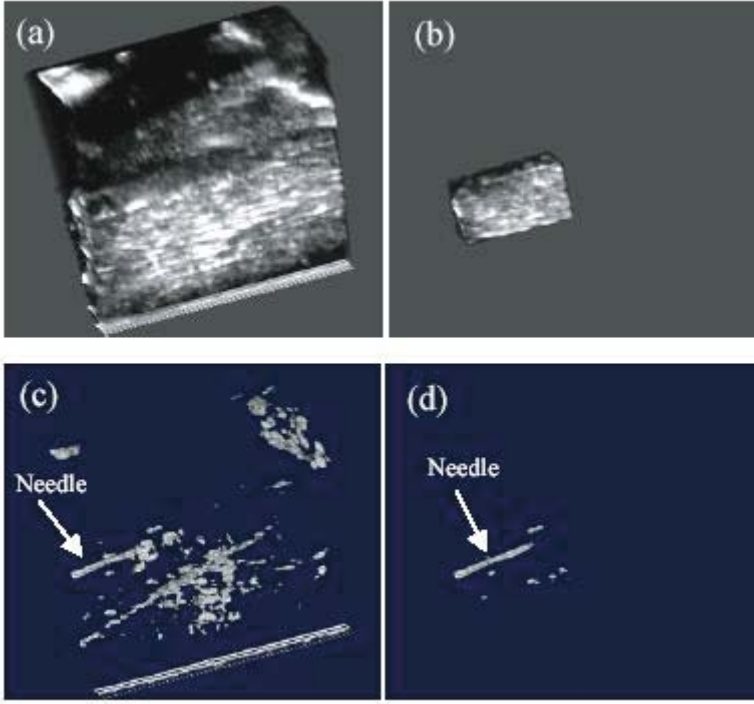


Figure 8.9. Comparison of volume cropped and rendered images of a turkey breast phantom. (a) The MPR display of 3D US turkey phantom image; (b) Cropped volume of (a); (c) Rendered image of (a); (d) rendered image of (b).

basis vectors of a right-handed 3D Cartesian coordinate system (Figure 8.10). We then form two projection images in the orthogonal directions \mathbf{Q} and $\mathbf{R}' = -\mathbf{R}$.

For the 2D projection image projected in the direction \mathbf{Q} , i.e., with $\hat{u} \times \hat{v} = -\mathbf{Q}$, we choose $\hat{u} = \mathbf{P}$. Then $\hat{v} = \hat{u} \times \mathbf{Q} = \mathbf{R}$. From the 2D needle segmentation, we then find that the endpoints of the estimated projected needle vector \mathbf{L} are

$$(p_n, r_n)_Q = (u_n, v_n), \quad n = 1, 2. \quad (8.12)$$

For the 2D projection image projected in the direction $\mathbf{R}' = -\mathbf{R}$, i.e., with $\hat{u} \times \hat{v} = -\mathbf{R}' = \mathbf{R}$, we again choose $\hat{u} = \mathbf{P}$. Then $\hat{v} = \hat{u} \times \mathbf{R}' = -\hat{u} \times \mathbf{R} = \mathbf{Q}$. From the 2D needle segmentation, we then find that the endpoints of the estimated projected needle vector \mathbf{L} are:

$$(p_n, q_n)_{R'} = (u_n, v_n), \quad n = 1, 2 \quad (8.13)$$

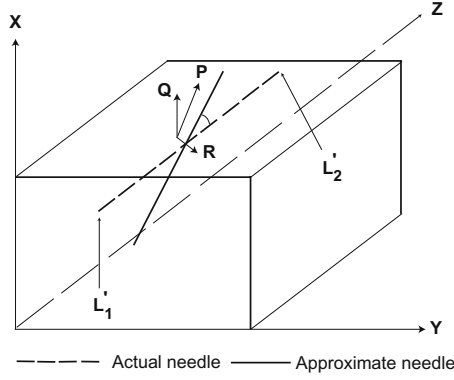


Figure 8.10. 3D coordinate systems used in 3D needle segmentation.

We now suppose that a known point $\mathbf{O} = (x_0, y_0, z_0)$ in the cropped volume (e.g., its center) is projected onto the origin of the u - v plane in both projection images, and define

$$p_n = (p_{nQ} + p_{nK})/2, \quad n = 1, 2, \quad (8.14)$$

$$q_n = q_{nR'}, \quad n = 1, 2, \quad (8.15)$$

$$r_n = r_{nQ}, \quad n = 1, 2. \quad (8.16)$$

Then, the estimated 3D coordinates of the needle's endpoints are given by:

$$\mathbf{L}_n'' = \mathbf{O} + p_n \mathbf{P} + q_n \mathbf{Q} + r_n \mathbf{R}, \quad n = 1, 2, \quad (8.17)$$

and the estimated length of the needle is given by:

$$\mathbf{L}_0'' = |\mathbf{L}_2'' - \mathbf{L}_1''|. \quad (8.18)$$

Finally, the errors δ_n in \mathbf{L}_n , $n = 0, 1, 2$, are given by

$$\delta_0 = |\mathbf{L}_0'' - \mathbf{L}_0'|, \quad (8.19)$$

$$\delta_n = |\mathbf{L}_n'' - \mathbf{L}_n'|, \quad n = 1, 2, \quad (8.20)$$

where the actual needle endpoints \mathbf{L}_1' and \mathbf{L}_2' and needle length $\mathbf{L}_0' = |\mathbf{L}_2' - \mathbf{L}_1'|$ are determined by manually segmenting the needle in the 3D US image.

8.7 Brachytherapy Seed Segmentation in 3D US Images

After completing the brachytherapy seed implantation procedure, the seeds' actual locations must be evaluated by CT or MRI imaging. Using this information, a dosimetric analysis (post-plan) is then performed to determine

whether the dose coverage of the implant is satisfactory. If it is not, then additional seeds can be implanted in the underdosed area. However, if the seed placement could be evaluated with a 3D US imaging system (the same system used to provide image guidance during the procedure), then a post-plan could be performed immediately, and the additional seeds could then be implanted intraoperatively as an extension of the regular procedure, instead of in a separate procedure after the post-plan CT or MRI examination is completed. Moreover, if 3D US image guidance with simultaneous seed placement verification could be carried out, the treatment plan could be continuously adjusted during the procedure, as the seeds are implanted, thereby minimizing the required number of needle insertions, and maximizing the effectiveness of the radiation therapy.

However, performing seed segmentation in 3D US images is extremely difficult, for four reasons: First, calcifications and other small structures with high echogenicity can mimic the bright appearance of a brachytherapy seed in an US image, making positive seed identification difficult, unlike the situation in a CT or MRI image (see Figure 8.11). Second, many seeds are implanted into the prostate, typically 80-100, unlike the situation described in the preceding section, where a single needle is being segmented. Third, because a seed is cylindrically shaped (about 0.8 mm in diameter and 4 mm in length, similar to a grain of rice), the brightness in the 3D US image can vary greatly, depending on its orientation relative to the ultrasound transducer (being much brighter when the seed is oriented parallel to the transducer, due to specular reflection). Fourth, the images of the seeds are superimposed on a highly cluttered US image background.

8.7.1 Volume Cropping

By using the 3D prostate segmentation described in Section 8.5, we can crop the 3D US image to a volume that contains only the prostate and its immediate surroundings, where all the radioactive seeds are located. This not only greatly eases the task of seed segmentation, but also saves a great deal of computational time.

8.7.2 Adaptive Thresholding

The voxels in the cropped volume are segmented using an adaptive thresholding technique. Suppose that the 3D US image has N gray levels, and let $\{h(n), n = 0, \dots, N - 1\}$ be the gray-level histogram of the cropped volume. Then, because the images of the seeds are bright, the adaptive threshold T is defined as

$$T = \max \left\{ t \mid \sum_{n=t}^{255} h(n) \geq n_0, t = 0, 1, \dots, 255 \right\}, \quad (8.21)$$

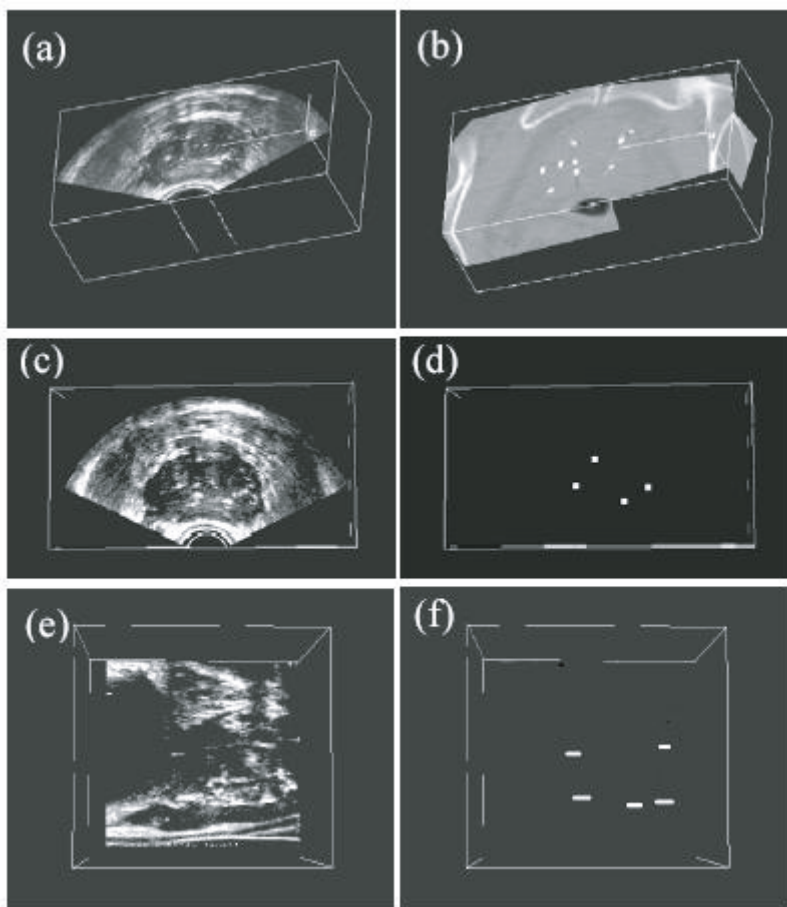


Figure 8.11. Seed segmentation results: (a) and (b) are the 3D US and the corresponding CT image, displayed using the MPR technique. The size of the 3D US image is 383,383,246 voxels; (c) is a lateral slice, and (e) is a sagittal slice of the 3D US image; (d) and (f) are the seed segmentation results of (c) and (e), with black background and white seeds.

where n_0 is the number of seed candidates. In implementing this technique, the value of n_0 must be chosen carefully. It must be large enough to ensure that the seed candidates include as many of the seeds as possible (for a high detection rate), but small enough to exclude as many false candidates as possible (for a low false positive rate). A suitable value for n_0 is 1% of the number of voxels in the cropped volume. The cropped volume is converted to a binary image, with the voxels whose gray levels equal or exceed T being assigned a value of 1, and the remaining voxels a value of 0.

8.7.3 Seed Candidate Extraction

In the binary image obtained by adaptive thresholding, each connected group of voxels is generally considered to be a seed candidate. Morphological operations are used to separate or join these groups and may be employed when deemed appropriate.

8.7.4 Seed Identification

Each seed candidate is labeled and analyzed to determine its size s in voxels, its mean gray-level \bar{I} , the direction of its principal axis, and the angle θ between the principal axis and the planned seed line. Then, the candidates are classified according to three criteria. Candidates which meet all these criteria are identified as seeds and the rest are classified as nonseed bright objects, such as calcifications or other small echogenic structures. The criteria are:

1. $s_{\min} \leq s \leq s_{\max}$,
2. $\bar{I} \geq I_{\min}$,
3. $\theta \leq \theta_{\max}$,

where s_{\min} is determined empirically and s_{\max} is calculated from the physical dimensions of the seed and the voxel dimensions of the 3D US image; I_{\min} is found from a set of manually segmented seed images; and θ_{\max} depends on the statistical distribution of θ in a typical line cluster of seed candidates. In our case, we used $\theta_{\max} = 12^\circ$.

Some of our seed segmentation results are shown in Figure 8.11. Figures 8.11(a) and (b) are views of the 3D US image and the corresponding CT image, both displayed using the multiplanar reformatting technique. These images demonstrate the 3D US image contains much lower seed contrast and much higher background complexity, compared to the CT image. In its current form, the seed segmentation algorithm has a seed detection rate of about 80%, and a false positive rate of about 11 %.

8.8 Conclusion

Three-dimensional ultrasound imaging is becoming a mature technology that has been used in many different diagnostic and therapeutic/surgical applications. In this chapter we described the principles of 3D US imaging and its applications in image-guided prostate brachytherapy. Our focus has been on the discussion of 3D segmentation of the prostate, needle and seeds to be used in 3D US-guided prostate brachytherapy. Additional developments are still required to exploit the full potential of 3D US imaging capabilities. For example, the development of a real-time 3D US imaging system would increase the efficiency and accuracy of needle biopsies. Also, improving 3D visualization techniques, so that they are more intuitive, would allow physicians

to become more comfortable with advanced computational tools, resulting in the wider availability of this technology. Finally, faster, more accurate, and less variable segmentation and classification techniques using 3D US images would allow better estimation of organ and tumor volumes, resulting in improved treatment planning and therapy monitoring of patients.

References

- [1] Fenster, A., Downey, D.B., Cardinal, H.N.: Topical review: Three-dimensional ultrasound imaging. *Phys. Med. Biol.* **46** (2001) R67–R99
- [2] Nelson, T.R., Downey, D.B., Pretorius, D.H., Fenster, A.: Three-dimensional ultrasound. Lippincott-Raven, Philadelphia (1999)
- [3] Fenster, A., Downey, D.B.: Three-dimensional ultrasound imaging: A review. *EEE Engineering in Medicine and Biology* **15** (1996) 41–51
- [4] Smith, S.W., Trahey, G.E., von Ramm, O.T.: Two-dimensional arrays for medical ultrasound. *Ultrason Imaging* **14** (1992) 213–33
- [5] Tvon Ramm, O.T., Smith, S.W., Pavy, H.G.J.: High-speed ultrasound volumetric imaging system. part ii. parallel processing and image display. *IEEE Trans. Ultrason Ferroelec Freq. Contr.* **38** (1991) 109–115
- [6] Downey, D.B., Fenster, A.: Three-dimensional power doppler detection of prostatic cancer. *Am. J. Roentgenol* **165** (1995a) 741
- [7] Downey, D.B., Fenster, A.: Vascular imaging with a three-dimensional power doppler system. *Am. J. Roentgenol* **165** (1995b) 665–8
- [8] Silverman, R.H., Rondeau, M.J., Lizzi, F.L., Coleman, D.J.: Three-dimensional high-frequency ultrasonic parameter imaging of anterior segment pathology. *Ophthalmology* **102** (1995) 837–43
- [9] Guo, Z., Fenster, A.: Three-dimensional power doppler imaging: a phantom study to quantify vessel stenosis. *Ultrasound Med. Biol.* **22** (1996) 1059–69
- [10] Picot, P.A., Rickey, D.W., Mitchell, R., Rankin, R.N., Fenster, A.: Three-dimensional color doppler imaging of the carotid artery. In: *SPIE Proceedings: Image Capture, Formatting and Display. Volume 1444.*, Atlanta, GA (1991) 206–213
- [11] Picot, P.A., Rickey, D.W., Mitchell, R., Rankin, R.N., Fenster, A.: Three-dimensional color doppler imaging. *Ultrasound Med. Biol.* **19** (1993) 95–104
- [12] Pretorius, D.H., Nelson, T.R., Jaffe, J.S.: Three-dimensional sonographic analysis based on color flow doppler and grayscale image data: a preliminary report. *J. Ultrasound Med.* **11** (1992) 225–32
- [13] Bamber, J.C., Eckersley, R.J., Hubregtse, P., Bush, N.L., Bell, D.S., Crawford, D.C.: Data processing for 3D ultrasound visualization of tumour anatomy and blood flow. *SPIE* **1808** (1992) 651–663

- [14] Guo, Z., Moreau, M., Rickey, D.W., Picot, P.A., Fenster, A.: Quantitative investigation of in vitro flow using three-dimensional color doppler ultrasound. *Ultrasound Med. Biol.* **21** (1995) 807–16
- [15] Cardinal, H.N., Gill, J.D., Fenster, A.: Analysis of geometrical distortion and statistical variance in length, area, and volume in a linearly scanned 3d ultrasound image. *IEEE Transactions on Medical Imaging* **19** (2000) 632–651
- [16] Delabays, A., Pandian, N.G., Cao, Q.L., Sugeng, L., Marx, G., Ludomirski, A., Schwartz, S.L.: Transthoracic real-time three-dimensional echocardiography using a fanlike scanning approach for data acquisition: methods, strengths, problems, and initial clinical experience. *Echocardiography* **12** (1995) 49–59
- [17] Downey, D.B., Fenster, A.: Three-dimensional orbital ultrasonography. *Can. J Ophthalmol* **30** (1995c) 395–8
- [18] Elliot, T.L., Downey, D.B., Tong, S., McLean, C.A., Fenster, A.: Accuracy of prostate volume measurements in vitro using three-dimensional ultrasound. *Acad. Radiol.* **3** (1996) 401–6
- [19] Tong, S., Downey, D.B., Cardinal, H.N., Fenster, A.: A three-dimensional ultrasound prostate imaging system. *Ultrasound Med. Biol.* **22** (1996) 735–46
- [20] Chin, J.L., Downey, D.B., Mulligan, M., Fenster, A.: Three-dimensional transrectal ultrasound guided cryoablation for localized prostate cancer in nonsurgical candidates: a feasibility study and report of early results. *J. Urol.* **159** (1998) 910–4
- [21] Tong, S., Cardinal, H.N., Downey, D.B., Fenster, A.: Analysis of linear, area and volume distortion in 3d ultrasound imaging. *Ultrasound Med. Biol.* **24** (1998) 355–73
- [22] Brinkley, J.F., McCallum, W.D., Muramatsu, S.K., Liu, D.Y.: Fetal weight estimation from lengths and volumes found by three-dimensional ultrasonic measurements. *J. Ultrasound Med.* **3** (1984) 163–8
- [23] King, D.L., King, D.J., Shao, M.Y.: Three-dimensional spatial registration and interactive display of position and orientation of real-time ultrasound images. *J. Ultrasound Med.* **9** (1990) 525–32
- [24] Bonilla-Musoles, F., Raga, F., Osborne, N.G., Blanes, J.: Use of three-dimensional ultrasonography for the study of normal and pathologic morphology of the human embryo and fetus: preliminary report. *J. Ultrasound Med.* **14** (1995) 757–65
- [25] Detmer, P.R., Bashein, G., Hodges, T., Beach, K.W., Filer, E.P., Burns, D.H., Strandness, D.E.J.: Three-dimensional ultrasonic image feature localization based on magnetic scanhead tracking: in vitro calibration and validation. *Ultrasound Med. Biol.* **20** (1994) 923–36
- [26] Ganapathy, U., Kaufman, A.: 3d acquisition and visualization of ultrasound data. In: *SPIE Proc. Of Visualization in biomedical computing SPIE. Volume 1808.* (1992) 535–545

- [27] Gilja, O.H., Detmer, P.R., Jong, J.M., Leotta, D.F., Li, X.N., Beach, K.W., Martin, R., Strandness, D.E.J.: Intragastric distribution and gastric emptying assessed by three-dimensional ultrasonography. *Gastroenterology* **113** (1997) 38–49
- [28] Hughes, S.W., D’Arcy, T.J., Maxwell, D.J., Chiu, W., Milner, A., Saunders, J.E., Sheppard, R.J.: Volume estimation from multiplanar 2D ultrasound images using a remote electromagnetic position and orientation sensor. *Ultrasound Med. Biol.* **22** (1996) 561–72
- [29] Leotta, D.F., Detmer, P.R., Martin, R.W.: Performance of a miniature magnetic position sensor for three-dimensional ultrasound imaging. *Ultrasound Med. Biol.* **23** (1997) 597–609
- [30] Nelson, T.R., Pretorius, D.H.: Visualization of the fetal thoracic skeleton with three-dimensional sonography: a preliminary report. *Am. J. Roentgenol* **164** (1995) 1485–8
- [31] Tuthill, T.A., Krucker, J.F., Fowlkes, J.B., Carson, P.L.: Automated three-dimensional us frame positioning computed from elevational speckle decorrelation. *Radiology* **209** (1998) 575–82
- [32] Chin, J.L., Downey, D.B., Onik, G., Fenster, A.: Three-dimensional prostate ultrasound and its application to cryosurgery. *Tech. Urol.* **2** (1996) 187–93
- [33] Kirbach, D., Whittingham, T.A.: Three-dimensional ultrasound - the Kretztechnik-Voluson approach. *European J. Ultrasound* **1** (1994) 85–89
- [34] Zosmer, N., Jurkovic, D., Jauniaux, E., Gruboeck, K., Lees, C., Campbell, S.: Selection and identification of standard cardiac views from three-dimensional volume scans of the fetal thorax. *J Ultrasound. Med.* **15** (1996) 25–32
- [35] Levoy, M.: Volume rendering, a hybrid ray tracer for rendering polygon and volume data. *IEEE Computer Graphics and Applications* **10** (1990) 33–40
- [36] Garfinkel, L., Mushinski, M.: Cancer incidence, mortality, and survival trend in four leading sites. *Stat. Bull.* **75** (1994) 19–27
- [37] Nag, S.: Principles and Practice of Brachytherapy. Futura Publishing Company, Inc, Amonk, NY (1997)
- [38] Richard, W.D., Grimmell, C.K., Bedigian, K., Frank, K.J.: A method for 3D prostate imaging using transrectal ultrasound. *Comput. Med. Imaging Graphics* **17** (1993) 73–79
- [39] Richard, W.D., Keen, C.G.: A method for 3D prostate imaging using transrectal ultrasound. *Comput. Med. Imaging Graphics* **20** (1996) 131–140
- [40] Aarnink, R.G., Giesen, R.J.B., Huynen, A.L., Debruyne, F.M.J., Wijkstra, H.: Automated prostate volume determination. In: *Proc. of IEEE Eng. Med. Biol. Soc. Volume 14.* (1992) 2146–2147
- [41] Aarnink, R.G., Giesen, R.J.B., Huynen, A.L., De la Rosette, J.J., Debruyne, F.M.J., Wijkstra, H.: A practical clinical method for contour de-

- termination in ultrasonographic prostate images. *Ultrasound Med. Biol.* **20** (1994) 705–717
- [42] Aarnink, R., Giesen, R.J.B., Huynen, A.L., De la Rosette, J.J., Debruyne, F.M.J., Wijkstra, H.: Automated prostate volume determination with ultrasonographic imaging. *J. Urol.* **153** (1995) 1549–1554
- [43] Aarnink, R.G., Giesen, R.J.B., Huynen, A.L., De la Rosette, J.J., Debruyne, F.M.J., Wijkstra, H.: Edge detection in prostatic ultrasound images using integrated edges maps. *Ultrasonics* **36** (1998) 635–642
- [44] Liu, Y.J., Ng, W.S., Teo, M.Y., Lim, H.C.: Computerised prostate boundary estimation of ultrasound images using radial bas-relief method. *Med. Biol. Eng. Comput.* **35** (1997) 445–454
- [45] Kwok, C.K., Teo, M.Y., Ng, W.S., Tan, S.N., Jones, L.M.: Outlining the prostate boundary using the harmonics method. *Med. Biol. Eng. Comput.* **36** (1998) 768–771
- [46] Pathak, S.D., Aarnink, R.G., De la Rosette, J.J., Chalaria, V., Wijkstra, H., Haryror, D.R., Debruyne, F.M.J., Kim, Y.: Quantitative three-dimensional transrectal ultrasound (TRUS) for prostate imaging. In: *Proc. of SPIE. Volume 3335.* (1998) 83–92
- [47] Pathak, S.D., Chalaria, V., Haryror, D.R., Kim, Y.: Edge-guided delineation of the prostate in transrectal ultrasound images. In: *Proc. of the 1st Joint Meeting of the Biology Engineering Society and IEEE Engineering in Medicine and Biology Society, Atlanta, GA* (1999) 1056
- [48] Pathak, S.D., Chalaria, V., Haryror, D.R., Kim, Y.: Edge-guided boundary delineation in prostate in ultrasound images. *IEEE TMI* **19** (2000) 1211–1219
- [49] Knoll, C., Alcaniz, M., Grau, V., Monserrat, C., Juan, M.C.: Outlining of the prostate using snakes with shape restrictions based on the wavelet transform. *Pattern Recognition* **32** (1999) 1767–1781
- [50] Garfinkel, L., Mushinski, M.: A three-dimensional deformable model for segmentation of human prostate from ultrasound images. *Med. Phys.* **28** (2001) 2147–2153
- [51] Kass, M., Witkin, A., Terzopoulos, D.: Snakes: Active contour models. *International Journal of Computer Vision* **1** (1987) 321–331
- [52] Terzopoulos, D., Fleischer, K.: Deformable models. *The Visual Computer* **4** (1988) 306–331
- [53] Singh, A., Goldgof, D., Terzopoulos, D.: *Deformable Models in Medical Image Analysis.* IEEE Press, Los Alamitos, CA (1998)
- [54] McInerney, T., Terzopoulos, D.A.: A dynamic finite-element surface model for segmentation and tracking in multidimensional medical images with applications to cardiac 4D image analysis. *Computer Medical Imaging Graphics* **19** (1995) 69–83
- [55] McInerney, T., Terzopoulos, D.: Deformable models in medical image analysis: A survey. *Medical image Analysis* **1** (1996) 91–108

- [56] McInerney, T., Terzopoulos, D.: Topology adaptive deformable surfaces for medical image volume segmentation. *IEEE Transactions on Medical Imaging* **18** (1999) 840–850
- [57] McInerney, T., Terzopoulos, D.: T-snakes: Topology adaptive snakes. *Medical Image Analysis* **4** (2000) 73–91
- [58] Keeve, E., Kikinis, R.: Deformable modeling of facial tissue. In: *Proceedings of the First Joint BMES/EMBS Conference*. Volume 1.1. (1999) 502
- [59] Sitek, A., Klein, G.J., Gullberg, G.T., Huesman, R.H.: Deformable model of the heart with fiber structure. *IEEE Transactions on Nuclear Science* **49** (2002) 789–793
- [60] Metaxas, D.N., Kakadiaris, I.A.: Elastically adaptive deformable models. *IEEE Transactions on Medical Imaging* **24** (2002) 1310–1321
- [61] Miller, J.V., Breen, D.E., Lorensen, W.E., O’Bara, R.M., Wozny, M.J.: Geometrically deformable models: A method to extract closed geometric model from volume data. *Computer Graphics* **25** (91) 217–226
- [62] Lobret, S., Viergever, M.A.: A discrete dynamic contour model. *IEEE Trans. Med. Image* **14** (1995) 12–24
- [63] Ladak, H.M., Mao, F., Wang, Y., Downey, D.B., Steinman, D.A., Fenster, A.: Prostate boundary segmentation from 2D ultrasound images. *Med. Phys.* **27** (2000) 1777–1788
- [64] Gill, J.D., Ladak, H.M., Steinman, D.A., Fenster, A.: Accuracy and variability assessment of a semiautomatic technique for segmentation of the carotid arteries from three-dimensional ultrasound images. *Med Phys* **27** (2000) 1333–1342
- [65] Solina, F., Bajcsy, R.: Recovery of parametric models from range images: The case for superquadrics with global deformation. *IEEE Transactions on Pattern Analysis and Machine Intelligence* **12** (1990) 131–147
- [66] Schroeder, W.J., Martin, K.M., Avila, L.S., Law, C.C.: *The VTK Users Guide*. Kitware, Inc (1998)
- [67] Bonilla-Musoles, F., Raga, F., Osborne, N.G., Blanes, J.: Principal warps: Thin-plate splines and the decomposition of deformations. , *IEEE Trans. Pattern Analysis and Machine Intelligence* **11** (1989) 567–585
- [68] Lichtenbelt, B., Crane, R., Naqvi, S.: *Introduction to Volume Rendering*. Prentice-Hall, Upper Saddle River, NJ (1998)